

ALMA Band 7 Imaging and Analysis of the Luminous Infrared Galaxy ESO 203-IG001

MIGUEL MONTALVO^{1,2}, LORETO BARCOS-MUÑOZ³ AND DEVAKY KUNNERIATH³

¹*Department of Astronomy, University of California Berkeley, Berkeley, CA 94720, USA*

²*Physical Sciences Department, Diablo Valley College, Pleasant Hill, CA 94523, USA*

³*National Radio Astronomy Observatory, 520 Edgemont Road, Charlottesville, VA 22903, USA*

ABSTRACT

Local Ultra/Luminous Infrared Galaxies (U/LIRGs) host one of the best laboratories to study star formation in extreme environments. Specifically, U/LIRGs showing compact emission (concentrated within the central kpc), with extremely high obscuration, and high star formation rates may represent a brief transition stage between powerful starbursts and optically visible QSOs. We present Atacama Large Millimeter/submillimeter Array Band 7 (~340 GHz) observations of the dense gas tracers HCN (4-3) and HCO⁺ (4-3) in one of the most obscured local LIRG, ESO 203-IG001, that is part of the Great Observatories All-sky LIRG Survey, to map and extract physical properties of the circumnuclear interstellar medium, including its dense gas and dust components. We detect 337.7 GHz continuum emission with a 10.6 mJy integrated flux, contained within an ellipse with axes 158pc x 113pc. From the continuum emission, a value of $8.9 \times 10^7 M_{\odot}$ is calculated for the dust mass. The molecular gas mass is calculated to be $5.2 \times 10^9 M_{\odot}$ from the published CO luminosity of the galaxy. We find enhanced HCN emission, relative to HCO⁺, with a ratio of 1.97. This value is higher than in typical galaxies, but it is unclear if it is due to AGN presence as some studies suggest. We observe different kinematics between the rotating disks and observe tentative evidence of an outflow, but further analysis must be performed with deeper observations and using different tracers, to understand the dynamics of the galaxy better and verify our preliminary results.

1. INTRODUCTION

1.1 Background Information

Luminous Infrared Galaxies, or LIRGs, are a type of galaxy with large amounts of dust and gas surrounding its nucleus, making it highly obscured. This obscuration, combined with high star formation make LIRGs very bright in the infrared, due to emission from star formation being absorbed by the surrounding dust and then reemitted in the infrared. These galaxies are very compact with potential AGN presence, and they are usually at some stage of a gas rich-merger. LIRGs are defined to have an infrared luminosity of $L_{IR}[8 - 1000\mu m] > 10^{11} L_{\odot}$ and Ultra Luminous Infrared Galaxies (ULIRGs) of $L_{IR}[8 - 1000\mu m] > 10^{12} L_{\odot}$. They can be highly obscured, so that even mid infrared observations fail to show what lies inside the thick layer of dust. Therefore,

observations using longer wavelengths, like radio, are needed to penetrate the obscuring dust and map the physical structure of the circumnuclear interstellar medium (ISM). Studying these galaxies could help us understand star formation evolution as they are in different stages of gas-rich mergers.

One of the best samples to study mergers is the Great Observatories All-sky LIRG Survey (GOALS), a multiwavelength study of 202 low redshift Luminous Infrared Galaxies in the local universe at different merging stages (Armus et al. 2009). The obscuration mentioned above is clear in a flux-limited sub-sample of these U/LIRGs (see figure 1 adapted from Stierwalt, et al. 2013). The 10 galaxies in the top region of the plot stand out presenting extremely deep silicate absorption at 9.7 μm , weak Polycyclic Aromatic Hydrocarbon (PAH) emission, and an excess of warm

($T > 500$ K) dust, suggesting that the bulk of the obscuration, as well as the infrared luminosity, occurs very close to the buried nucleus (within 1 kpc), which is expected mostly in late-stage mergers. There are then, two other distinct populations in the plot that are well classified as powerful starbursts on the lower right and naked QSOs on the lower left.

In a model presented in Hopkins, et al. 2008, the Star Formation Rate (SFR) is plotted as a function of the phases of growth in a “typical” galaxy undergoing a gas-rich major merger. The model describes how SFR stays constant until they experience close interaction and the SFR gets enhanced in late-stage mergers. This sub-sample of highly obscured galaxies may represent a brief transition stage in the evolution of a gas-rich merger to an optically visible QSO. Atacama Large Millimeter/submillimeter Array (ALMA) is a unique tool with which we can penetrate the obscuring dust and map the physical structure and the dynamics of the circum-nuclear ISM at unprecedented sensitivity and resolution. If we can look through the obscuring dust, we could get information on the early stages of a developing QSO.

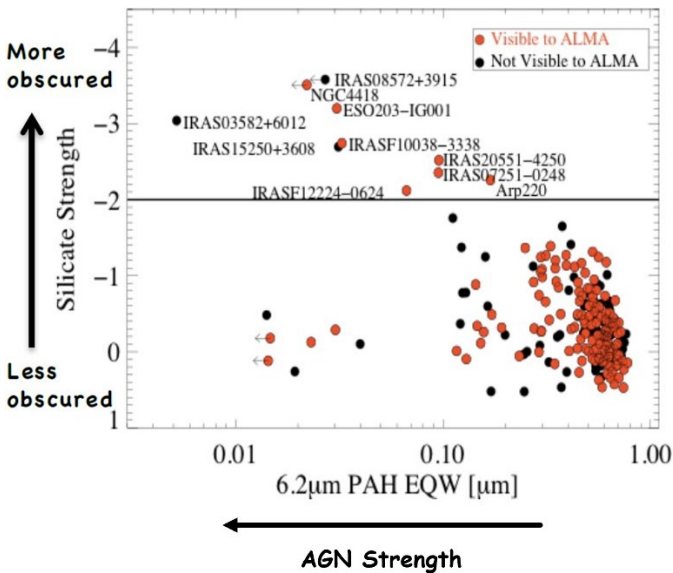


Figure 1 – Plot of $6.2\mu\text{m}$ PAH EQW vs. silicate depth for all LIRGs in GOALS. Red dots are galaxies visible to ALMA. The 10 most highly obscured (U)LIRGs, are labeled. As a group, these extremely obscured LIRGs may represent a brief transition phase between powerful starbursts (lower right) and naked QSOs (lower left).

1.2 Dense Gas Tracers

CO (1-0) is commonly used to trace the total molecular gas mass within a galaxy (e.g., Bolatto et al. 2013b); and so, it is used to locate star forming regions in a more general context. However, the relatively low critical density of CO ($n_{crit} \approx 10^2 \text{ cm}^{-3}$) means we also observe low-density molecular gas emission that is not directly involved in ongoing star formation. Gao & Solomon 2004a show a disperse relation between CO luminosity and star formation rate (as traced by $L_{IR}[8-1000 \mu\text{m}]$). In contrast, a linear correlation is observed between the HCN (1-0) and HCO+ (1-0) emission and star formation rate (e.g., Solomon et al. 1992; Gao & Solomon 2004a). This, plus the comparatively higher critical densities of the 1→0 lines ($n_{crit} \approx 10^6$ and 10^5 cm^{-3}) suggests the HCN and HCO+ emission trace the dense gas that is actively associated with ongoing star formation. With ALMA we can explore the morphologies and kinematics of the molecular gas over a large range in density. The HCN (4-3), CS (7-6) and HCO+ (4-3) lines provide a direct probe of the dynamics and morphology of the dense, circum-nuclear molecular gas (Scoville et al. 2015), and we can capture these lines with ALMA band 7.

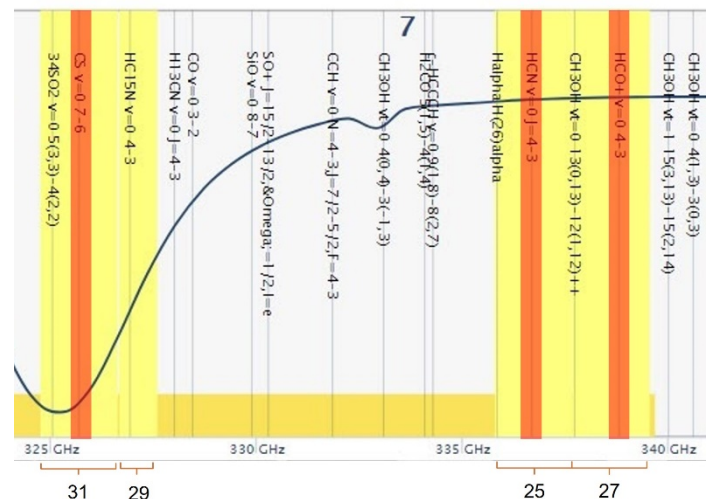


Figure 2 – Atmospheric transmission curve (blue line) for ALMA in band 7 showing the four spectral windows (yellow) for the observation setup targeting HCN (4-3), HCO+ (4-3) and CS (7-6) spectral lines (orange).

2. OBSERVATIONS AND DATA

2.1 Target ESO 203-IG001 and Observations

The ten most highly obscured (U)LIRGs are labeled in Figure 1. Only seven of those (in red) are galaxies visible to ALMA. Observations were carried out as part of project #2015.1.00708.S (PI: Armus) which includes four within those seven (U)LIRGs. The other three have been well-studied with ALMA. ESO 203-IG001 is one of the four observed sources, and the focus of this work. It is a LIRG with $L_{IR}[8 - 1000\mu m] = 7.24 \times 10^{11} L_{\odot}$ (Armus, et al. 2009) at a distance $D_L = 234 Mpc$ ($z = 0.0529$; angular scale: $1.13 \text{ kpc arcsec}^{-1}$). The SFR of this source, derived from the infrared luminosity and using equation 15 from Murphy et al. 2012, is $88 M_{\odot} yr^{-1}$. This is normal for U/LIRGs and very high compared to spiral galaxies like our Milky Way with an $SFR = 3 - 4 M_{\odot} yr^{-1}$. The observation was done with 11.1 min on-source time and baseline lengths between 15.1m and 2.5km. The observing setup consisted of four independent spectral windows: each tuned to the redshifted frequencies of HCN (4-3), HCO+ (4-3), CS (7-6) and one centered at 327.1 GHz. The three spectral line windows had bandwidths of 1.875GHz and the last one had a bandwidth of 937.5MHz.

The atmospheric transmission curve for ALMA is shown in Figure 2. For spectral windows 29 and 31, the atmospheric transmission is poor and therefore the spectral windows are noisier. Because of this, I decided not to include these two spectral windows for the continuum imaging and only work with spectral windows 25 and 27, imaging the HCN (4-3) and HCO+ (4-3) spectral lines and the continuum emission from the line free channels in these two spectral windows.

2.2 Data reduction

Observations were calibrated and imaged using Common Astronomy Software Applications (CASA, McMullin et al. 2007). The data products were downloaded from the ALMA Archive and the script for PI was run to restore the calibrated measurement set in CASA v.4.7.0-1.

Data was imaged in CASA v. 5.6.1-8 using the task *tclean* with Briggs weighting (robust=0.5; Briggs

1995) and a pixel size of 0.01 arcsec. The resulting resolution of the data cubes was $0.150'' \times 0.12''$ ($\sim 170 \text{ pc} \times 135 \text{ pc}$) with rms sensitivity (σ) of $0.15 \text{ mJy beam}^{-1}$ at 3.3 km s^{-1} spectral resolution. Continuum emission was mapped by flagging spectral line emission channels. Dirty image cubes were created to identify the line-free channels and then, the CASA task *uvcontsub* was used to create a continuum-subtracted measurement set by subtracting a linear baseline fit to the line-free channels, which we then imaged using *tclean* to create continuum-free line cubes. All the rest frequencies were obtained from Splatalogue website, using 354.505 GHz for HCN (4-3), 356.734 GHz for HCO+ (4-3), and 342.882 GHz for CS (7-6).

3. RESULTS AND DISCUSSION

We followed a similar analysis as it was done in Privon et al. 2017 with IRAS 13120-5453 as they observed the same spectral lines that this project did. We determined dust mass from the continuum emission and star formation rate from the infrared luminosity. The spectral line data cubes were analyzed to determine integrated fluxes and sizes. We also generated moment maps for kinematic analysis using the CASA task *immoments*, clipping them at 3σ .

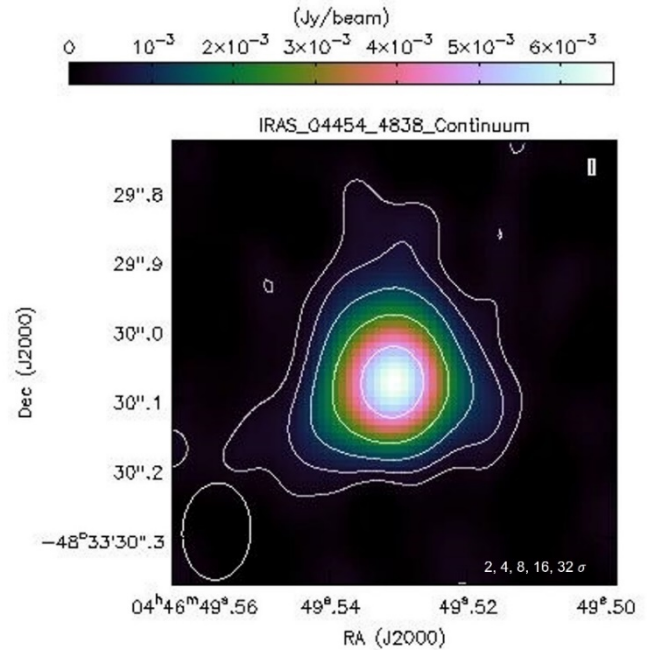


Figure 3 — Map of the 337.7 GHz continuum emission. Contours are laid on top of the image for values of $2^n \sigma$ for $n=1, 2, 3, 4$ and 5 , with $\sigma = 0.15 \text{ mJy}$.

3.1 Continuum Emission

The continuum provides an optically thin measure of the total ISM mass (Scoville et al. 2014). We detect 337.7 GHz continuum emission with a total flux (S) of 10.6 mJy. From this value, we calculated the dust mass using Equation 1, first presented in Casey et al. 2012.

$$M_{dust} = \frac{S_\nu D_L^2}{\kappa_\nu B_\nu(T)} \quad (1)$$

For the dust temperature we use $T = 33.2 K$, which is the mean in the (U)LIRG sample presented on Table 9 from U, Vivian et al. 2012. The mass absorption coefficient of the dust used $\kappa(333 \text{ GHz}) = 0.028 \text{ m}^2 \text{ kg}^{-1}$, is an estimate presented in Privon et al. 2017, and lastly the luminosity distance used is $D_L = 234 \text{ Mpc}$. This implies a dust mass of $8.9 \times 10^7 M_\odot$. If we assume a gas-to-dust mass ratio of 100 (Wilson et al. 2008), the ISM mass is then $\sim 9 \times 10^9 M_\odot$.

The CO intensity of the source (published in Mirabel, et al. 1990) was used to calculate the CO luminosity from equation in Solomon & Vander Bout 2005.

$$L'_{CO} = 23.5 \Omega_{s^*b} D_L^2 I_{CO} (1+z)^{-3} \quad (2)$$

From the CO luminosity we use equation in Solomon, et al. 1992 to convert the measured CO(J=1-0) flux to molecular gas mass, by assigning the U/LIRG value $\alpha_{CO} = 1.8 M_\odot$ from Herrero-Illana 2019.

$$M_{mol} = \alpha_{CO} L'_{CO} \quad (3)$$

The continuum emission implies a similar total ISM mass of $5.2 \times 10^9 M_\odot$ that is within the same order of magnitude of the estimated value from the dust mass, and therefore consistent with it. The detected continuum emission is contained within an ellipse with axes of $0.14'' \times 0.10''$ (158pc x 113pc; Figure 3). The distribution of the emission is well represented by a 2D Gaussian with a beam-deconvolved size (FWHM) of $0.11'' \times 0.08''$ (126pc x 93pc) at a PA of 96° and is marginally resolved.

3.2 Dense gas tracers

Emission from HCN (4–3) and HCO+ (4–3) was detected (Figure 4). We did not see clear evidence for

strong emission of the $v_2 = 1f$ HCN (4–3) vibrational transition. The integrated emission for both spectral lines is presented in Figure 5. The integrated flux was calculated in two ways.

First, the spectral profile was extracted using a circular aperture around the emission with a diameter of 1 arcsec, and the package *spectral_cube* was used to extract the spectral axis. The spectral profile was then fitted to a gaussian using the function *modeling* in *astropy*, with the model *Gaussian1D*. The gaussian fit was then used to calculate the integrated flux of HCN and HCO+ by taking the integral of the function with a cut in velocities to only include the channels where there was emission ($14698 < v < 15492 \text{ km/s}$ and $14678 < v < 15469 \text{ km/s}$ respectively).

Second, a 2D gaussian fit was performed on the integrated emission map (moment0) using the CASA task *imfit*. The results of both methods are presented in Table 1. The residuals from the gaussian fit were recovered for both spectral lines. The integrated fluxes, calculated using the two methods, differ from each other, since the one from the spectral profile includes fluxes in a larger aperture than the fit region, which are found in the residuals.

The HCN/HCO+ ratio was calculated using the integrated flux of each spectral line emission. The value obtained was 1.97. This ratio is higher than the value for typical galaxies, and that enhancement has been suggested to be due to outflow presence. People claim those outflows have to be AGN driven, but it is unclear if that is the case for this galaxy.

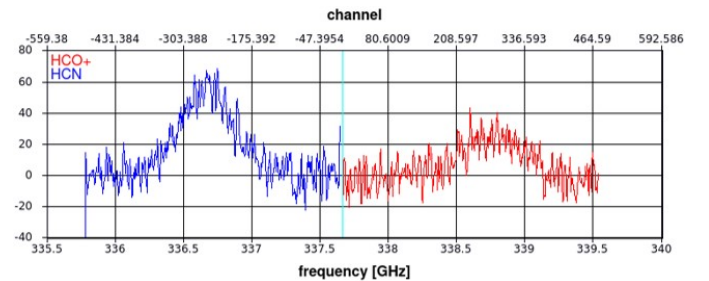


Figure 4 — Integrated spectra from ALMA observations of HCN (4–3) and HCO+ (4–3), continuum-subtracted and measured from a 1 arcsec diameter circular region centered on the nucleus

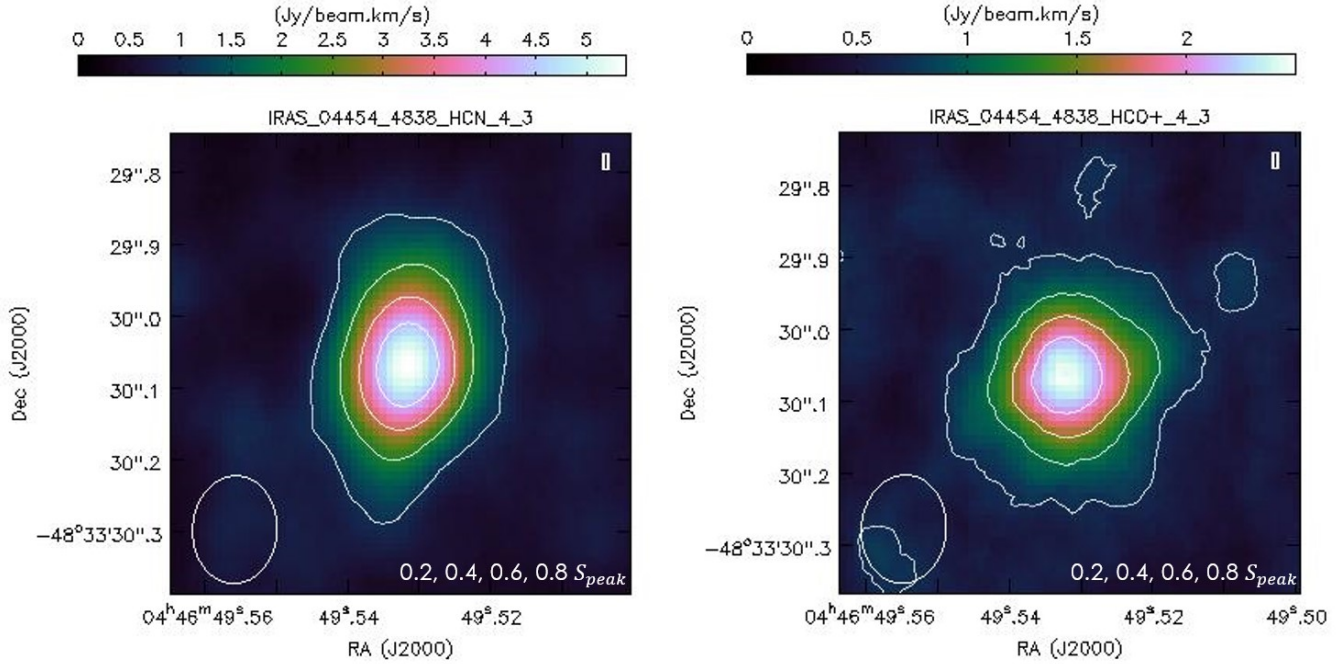


Figure 5 – Left: HCN (4–3) integrated emission map. Right: HCO+ (4–3) integrated emission map. Contours are laid on top of the images for fractions of the peak flux (0.2, 0.4, 0.6 and 0.8) respectively. HCO+ presents a more extended emission than HCN.

Table 1. Properties of HCN and HCO+ in the circumnuclear ISM

	HCN (4-3)	HCO+ (4-3)
Rest Frequency [GHz]	354.5	356.7
Peak Flux [Jy/beam·km/s]	5.4	2.5
Integrated Flux from 1" Circular Aperture [Jy·km/s]	23.3	11.8
Integrated Flux from 2D Gaussian Fit [Jy·km/s]	14.6	8.7
Clean Beam Size ["] / [pc]	0.15 x 0.12 / 170 x 136	0.15 x 0.12 / 170 x 136
Beam-Deconvolved Image Size ["] / [pc]	0.25 x 0.16 / 278 x 180	0.27 x 0.23 / 304 x 256
Position Angle [°]	163	148

The major axis of rotation in the disks can be deduced from the orientation of the velocity gradient observed in the mean velocity (moment 1) map. Two distinct rotation orientations can be seen between HCN and HCO+. For HCN is set at a position angle of 53.2° and for HCO+ is set at 93.8°. This difference could be due to different factors; for example, the different chemistry between the two molecules, and an analysis of radiative transfer effects.

From the velocity dispersion (moment 2) map, it can be observed that the peak dispersion velocity is off centered, and the maximum velocity dispersion is perpendicular to the major axis of rotation for both

spectral lines relatively. It is important to notice that the velocity dispersion has a direction perpendicular to the major axis of rotation for each molecule respectively. We would expect for a rotational motion that the velocity dispersion peaks at the center, but instead we observe a peak that is off-centered. This could imply that there may be an outflow in the direction of the highest dispersion. Peculiarly, along those same directions we can see two obscured conical regions in the optical image of this galaxy taken from Hubble Space Telescope in I band (775 nm) (Figure 7). We added lines on top of the image to guide the eye in the direction of dispersion that aligns with the features observed in the optical image.

4. FUTURE WORK

More work needs to be done to discover what is going on inside the thick layer of dust in ESO 203-IG001. A kinematic analysis would allow to be sure that there is an outflow coming from the nucleus of the galaxy. Unfortunately, this source is not very bright, and the observation setup didn't allow for a high signal

to noise ratio. Therefore, it would be ideal to observe this galaxy for a longer period, to increase the signal to noise, and then obtain better images of the circumnuclear ISM. With deeper observations and using different tracers, we can understand the dynamics of the galaxy better and verify our preliminary results.

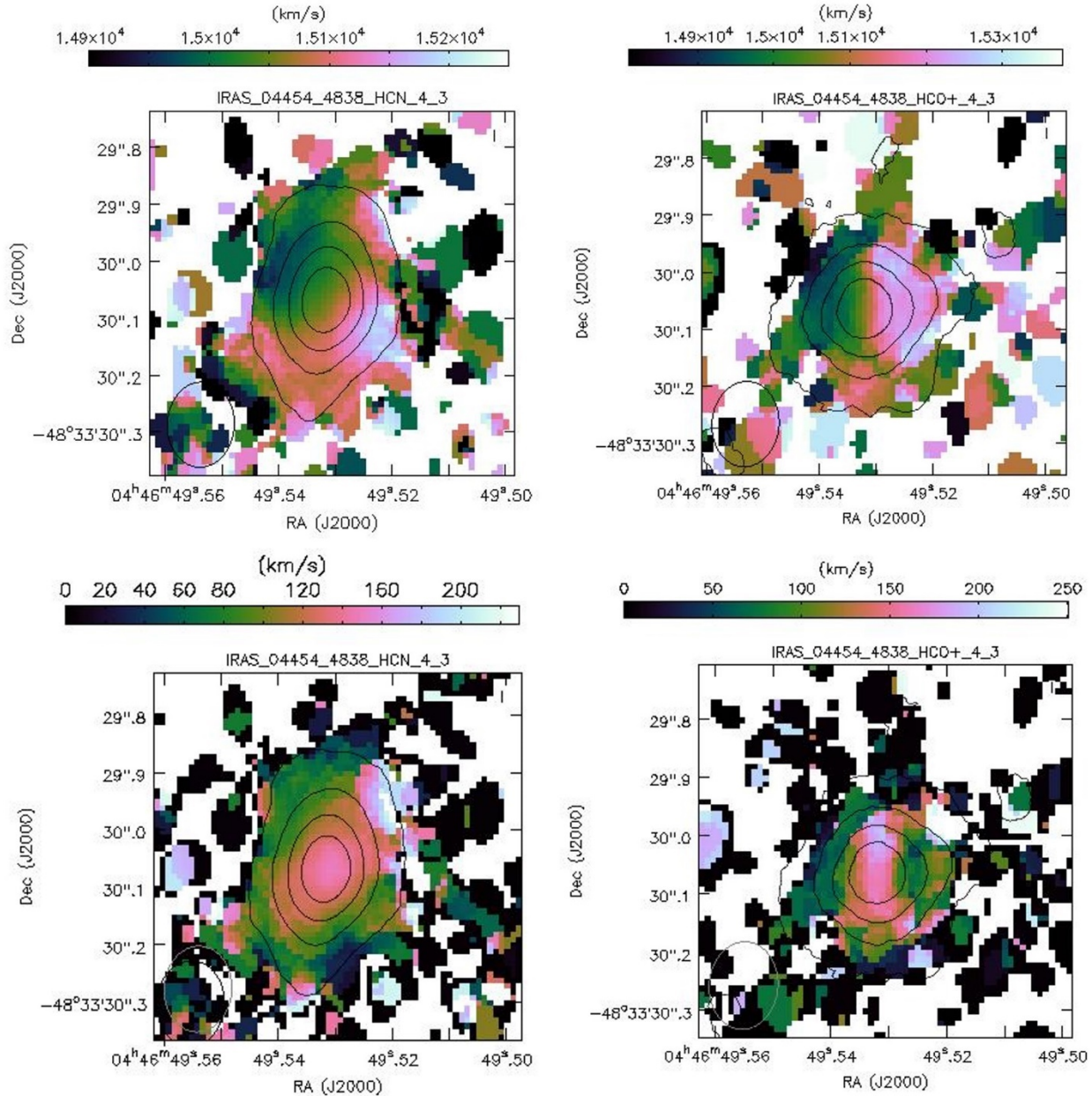


Figure 6 — Top row: intensity-weighted velocity map (moment 1) for HCN (4–3) (left) and HCO+ (4–3) (right). Bottom row: intensity-weighted velocity dispersion map (moment 2) for HCN (4–3) (left) and HCO+ (4–3) (right). Contours of the integrated emission are laid on top of each image with values of 0.2, 0.4, 0.6 and 0.8 S_{peak} respectively.

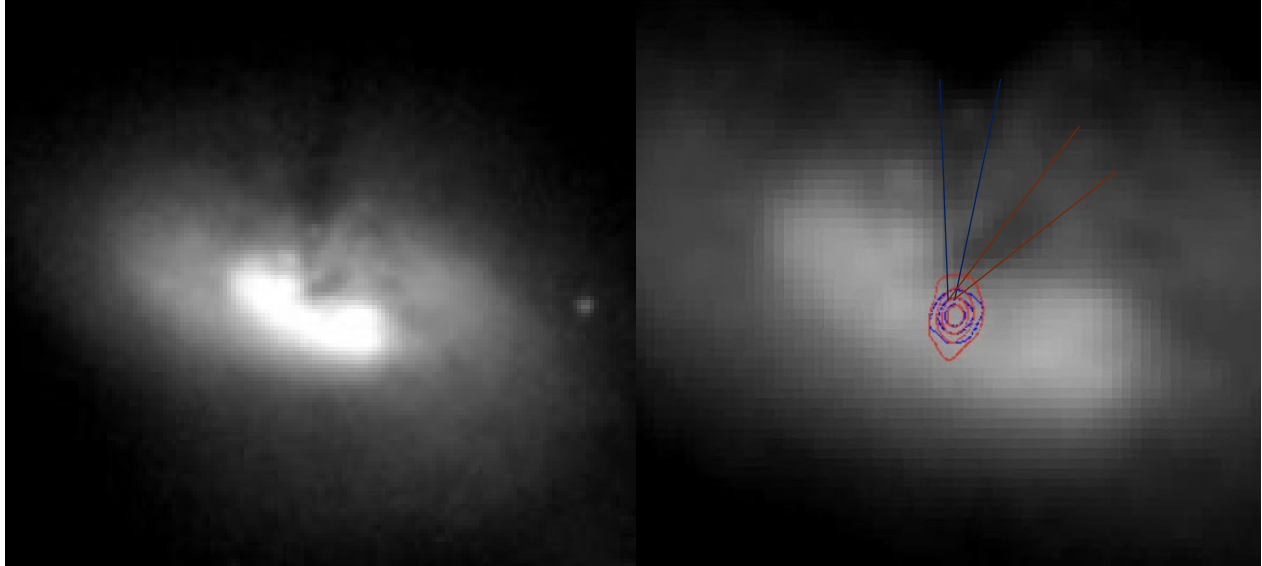


Figure 7 — Left: Hubble Space Telescope (HST) image in I band (775 nm) of ESO 203-GI001. Right: Integrated emission contours of HCN (red) and HCO+ (blue) with values of 0.2, 0.4, 0.6 and 0.8 S_{peak} respectively, laid on top of the HST image with lines coming from the center of the emission that represent tentative outflows that align with the maximum dispersion axis of each molecule.

5. REFERENCES

- Armus, L., Mazzarella, J.~M., Evans, A.~S., et al. 2009, *PASP*, 121, 559
- Bolatto, A. D., Wolfire, M., & Leroy, A. K. 2013b, *ARA&A*, 51, 207
- Briggs, D. 1995, PhD thesis, The New Mexico Institute of Mining and Technology
- Casey, C.~M., 2012, *MNRAS*, 425, 3094
- Gao, Y., & Solomon, P. M. 2004a, *ApJ*, 606, 271
- Herrero-Illana, R., Privon, G. C., Evans, A. S., et al. 2019, *A&A*, 628, A71
- Hopkins, P.F., et al. 2008, *ApJS*, 175, 356.
- McMullin, J. P., Waters, B., Schiebel, D., Young, W., & Golap, K. 2007, in *ASP Conf. Ser. 376, Astronomical Data Analysis Software and Systems XVI*, ed. R. A. Shaw, F. Hill, & D. J. Bell (San Francisco, CA: ASP), 127
- Mirabel, I.~F., Booth, R.~S., Garay, G., et al. 1990, *A&A*, 236, 327
- Murphy, E.~J., Bremseth, J., Mason, B.~S., et al. 2012, *ApJ*, 761, 97
- Privon, G.~C., Aalto, S., Falstad, N., et al. 2017, *ApJ*, 835, 213
- Scoville, N., Aussel, H., Sheth, K., et al. 2014, *ApJ*, 783, 84
- Scoville, N., Sheth, K., Walter, F., et al. 2015, *ApJ*, 800, 70
- Smith, B.~J., Wagstaff, P., Struck, C., et al. 2019, *AJ*, 158, 169
- Solomon, P. M., Downes, D., & Radford, S. J. E. 1992, *ApJL*, 387, L55
- Solomon, P.~M. & Vanden Bout, P.~A. 2005, *ARA&A*, 43, 677
- Stierwalt, S., Armus, L., Surace, J. A., et al. 2013, *ApJS*, 206, 1
- U, V., Sanders, D.~B., Mazzarella, J.~M., et al. 2012, *ApJS*, 203, 9
- Wilson, C. D., Petitpas, G. R., Iono, D., et al. 2008, *ApJS*, 178, 189